Ductile rupture of aluminum sheet materials

Jacques Besson[*][**] **— Wolfgang Brocks**[**]**— Olivier Chabanet**[**] **Dirk Steglich**[**]

[*] *Ecole des Mines de Paris Centre des Materiaux BP 87 Evry cedex F 91003*
besson@mat.ensmp.fr
[**] *Institute of Materials Research, GKSS Geesthacht D 21502, Germany*
{brocks,steglich,chabanet}@gkss.de

ABSTRACT. *This study deals with ductile tearing of Aluminum 2024 sheets. Tensile tests were conducted on smooth and notched specimens. They show that the plastic behavior is anisotropic. The crack path is slanted on moderately notched specimens whereas a normal to slant fracture transition is observed on severely notched samples. The damage behavior is modeled using the Rousselier model extended to account for plastic anisotropy. It is shown that the stress triaxiality can reach values up to 1.6. This shows, together with the slanted crack path, the importance of a 3D modeling. As these calculations require a large computational capacity, a relatively coarse mesh was used so that the load is overestimated. The experimental load could be reproduced changing the material parameters; in this case normal fracture is obtained. A finer mesh should be used to obtain simultaneously the correct crack path and load. To model cracking in large structures, a 2D plane stress cohesive zone model is used.*

RÉSUMÉ. *Cette étude concerne la déchirure ductile des tôles d'aluminium 2024. Des tests en traction ont été effectués sur des éprouvettes lisses et entaillées. Ils montrent que le comportement plastique est anisotrope. Le chemin de fissuration est en biseau sur les éprouvettes modérément entaillées alors qu'une transition d'une rupture normale à une rupture en biseau est observée sur les échantillons sévèrement entaillés. L'endommagement est modélisée en utilisant le modèle de Rousselier étendu pour tenir compte de l'anisotropie plastique. Il est montré que la triaxialité des contraintes peut atteindre des valeurs allant jusquà 1.6. Cela montre, avec le chemin de fissuration en biseau, l'importance d'une modélisation 3D. Comme ces calculs demandent une grande capacité de calcul, un maillage relativement grossier est employé de sorte que la charge est surestimée. La charge expérimentale pourrait être reproduite en changeant les paramètres matériaux ; dans ce cas on obtient une rupture normale. Un maillage plus fin devrait être utilisé pour obtenir en même temps le chemin de fissuration et la charge corrects. Pour modéliser la fissuration de grandes structures, une simulation 2D en contraintes planes utilisant le modèle de zone cohésive est proposée.*

KEYWORDS: *Aluminum 2024, sheet, ductile rupture, Rousselier model, cohesive zone model.*

MOTS-CLÉS : *Aluminium 2024, tôle, rupture ductile, modèle de Rousselier, modèle de zone cohésive.*

1. Introduction

A realistic assessment of the residual strength of cracked sheet materials (steel in pipeline or ships, aluminum in aircraft structures, zirconium in nuclear fuel components) requires methods to experimentally characterize crack growth resistance as well as numerical simulation tools capable of predicting crack initiation and propagation. Modeling can be done following two different strategies. On the one hand, the global approach to failure uses macroscopic rupture parameters such as the Crack Tip Opening Angle (CTOA) [GUL 99], the energy dissipation rate [TUR 92], the J–integral [RIC 68] or the J—Q parameters [O'D 92]. In general, these quantities suffer from a lack of transferability of fracture data from specimen to actual structures. On the other hand, the local approach to fracture provides a solution to the transferability problem by describing the degradation of the material using micromechanical state variables (e.g. void volume fraction, nucleated porosity ...). These models have been applied successfully to predict crack growth for thick walled components of structural steels [SUN 88, GUL 00] where a high stress triaxiality triggers the growth of voids as the main failure mechanism. Their application to thin walled high strength aluminum alloys faces some specific problems: (i) the stress triaxiality ratio in sheets is much lower than in thick structures whereas models of ductile damage have been established for high triaxialities; (ii) the fracture plane often shifts from a normal to a 45° inclined orientation to the applied load (fig. 2), (iii) rolled sheets generally show an anisotropic behavior with respect to both plastic hardening and void nucleating particles. However, fracture surfaces still show dimples which might result from growth of voids nucleated at second phase particles. Because of this, the application of models of ductile tearing seems to be promising.

In this work, the plastic and rupture behavior of thin aluminum sheets is characterized using smooth, blunt and sharp notched specimens. A 3D finite element modeling of fracture of small samples is performed using the Rousselier model [ROU 87]. The emphasis is put on the simulation of slant fracture. As this approach does not appear suitable to model crack extension in large structures, a 2D simulation using a cohesive zone model [NEE 90] is adopted.

2. Material and experiments

In this study, sheets of 1.73 mm thickness of a 2024 Al–alloy are investigated. The surface of the sheets is protected by a layer of 1050 aluminum whose thickness varies between 50 and 80 μm. The sheets are heat treated (T351 treatment). Several types of precipitates are present in the material [HER 98]: (i) coarse secondary phases containing iron and copper (size: 5 to 30 μm), (ii) $Al_{12}Mn_2Cu$ dispersoides (size: 20 to 500 nm), (iii) $Al_2(Cu,Mg)$ strengthening precipitates (size: a few nm).

The samples used to characterize the plastic and fracture behavior of the material are shown in figure 1. They include: smooth tensile bars, notched bars with U or V– notches and Kahn cracked specimens. All tests were performed with the load applied
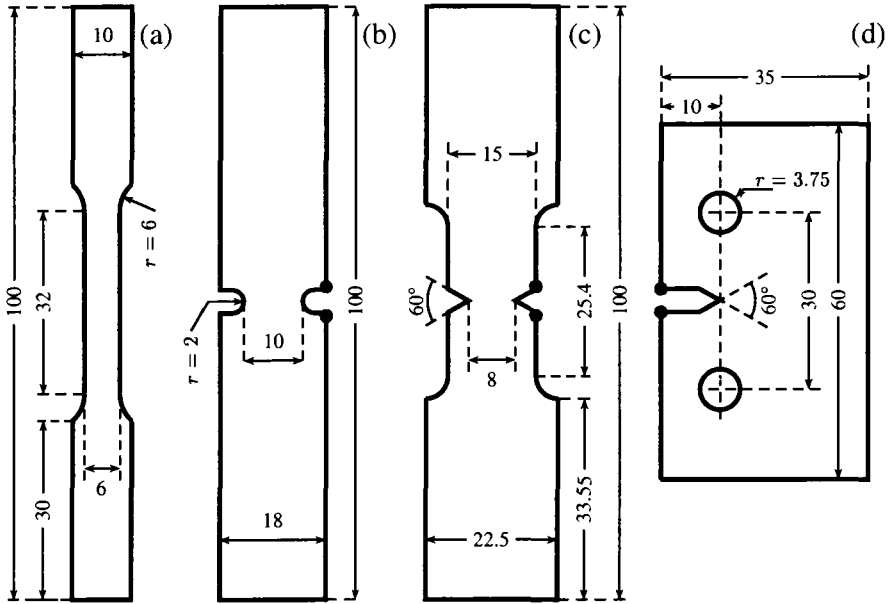
Figure 1. *Geometries of the specimens: (a) smooth tensile, (b) U–notch plate, (c) V–notch plate (notch radius: 0.25 mm), (d) Kahn specimen (notch radius: 0.06 mm, ASTM B-871–96). Gray dots indicate measurement points for the notch opening displacement $\Delta\delta$*

along the rolling direction (L); cracks propagate along the transverse direction (T). The short transverse direction will be referred to as S. Due to bending, stable crack growth is observed on Kahn samples whereas unstable rupture is obtained on the other specimens. Post–mortem measurements on tensile specimens outside the necking region have shown that the thickness reduction along the S—direction is larger than along the T—direction evidencing an anisotropic plastic behavior.

Fig. 2 shows the fracture surface of a V–notched specimen. Fracture is initiated at the middle of the notch where the fracture surface is normal to the loading direction (zone ① in fig. 2–(b)). This region forms a small triangle. Outside this zone, slant fracture in the L—S plane is observed. A closer examination of the fracture surfaces, shows void growth around the iron/copper particles. Void growth is more pronounced in the flat fracture region than in the slant fracture zones (② and ③ in fig. 2-(b)). Between these voids, small dimples, probably initiated on dispersoides or $Al_2(Cu,Mg)$ precipitates, are observed. Similar features were observed on Kahn specimens.

On tensile and U–notched specimens, the macroscopic fracture surface is entirely slanted (fig. 4, 5). An example of the microscopic fracture surface is shown on fig. 3. The rupture surface exhibits flat and smooth areas where small dimples cannot be
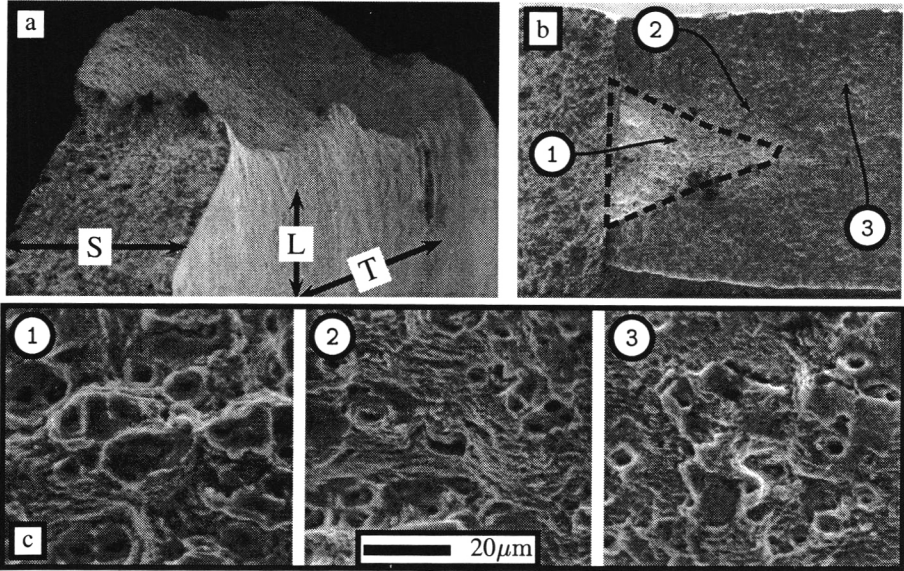
Figure 2. *Fractography (V–notch plate): (a) Macroscopic view showing the inclined crack path. (b) Macroscopic view showing (L direction) the flat crack initiation region (triangle). (c) Microscopic fracture faces corresponding to different regions of the crack path (1, 2 and 3; locations are indicated on (b))*

seen. This indicates a possible change in the fracture mechanisms between cracked or severely notched samples and specimens containing smooth geometrical defects. The proportion of smooth fracture zones increases in the case of the tensile specimens.
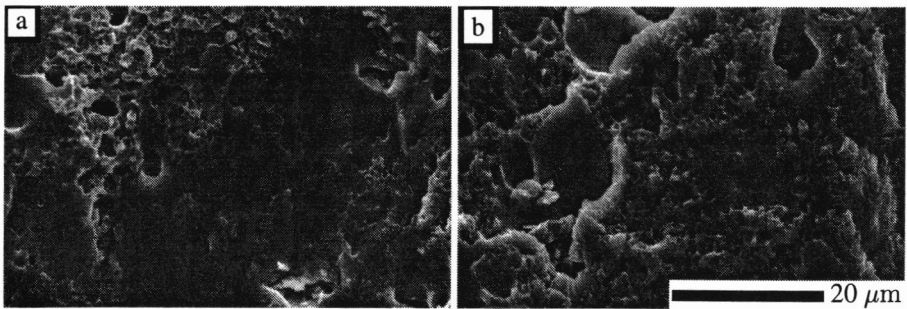
Figure 3. *Fracture surface of smooth (a) and U–notched specimens (b) exhibiting flat fracture zones*

3. Continuous damage mechanics: Rousselier model

3.1. *Constitutive equations*

Continuous damage mechanics (CDM) can be used to describe the rupture behavior of the material.   In this study, the Rousselier model has been employed [ROU 87]. The original model is extended to account for plastic anisotropy of the matrix material and damage nucleation.   A similar extension was used in [GRA 00] for the Gurson model. In that case the yield surface is expressed as:

$$\Phi = \frac{\sigma_H}{1 - f_t} + \sigma_1 D f_t \exp\left(\frac{\sigma_{kk}}{3(1 - f_t)\sigma_1}\right) - R(p).$$ [1]

σ_{kk} is the trace of the stress tensor $\underline{\sigma}$ and σ_H is the Hill equivalent stress defined by:

$$\sigma_H^2 = \frac{3}{2}\left(h_{\text{SS}}s_{\text{SS}}^2 + h_{\text{TT}}s_{\text{TT}}^2 + h_{\text{LL}}s_{\text{LL}}^2 + 2h_{\text{ST}}s_{\text{ST}}^2 + 2h_{\text{TL}}s_{\text{TL}}^2 + 2h_{\text{SL}}s_{\text{SL}}^2\right).$$ [2]

where s_{ij} are the components of the stress deviator. The coefficients h_{SS} ... are used to describe the plastic anisotropy. Using the deformation measurements and considering that the yield limit in the T–direction is 10% smaller than in the L–direction [HER 98, SIE 99] one gets: $h_{\text{LL}} = 0.79$, $h_{\text{TT}} = 1.16$, $h_{\text{SS}} = 1.68$. It was assumed that: $h_{\text{ST}} = h_{\text{TL}} = h_{\text{SL}} = 1$; this assumption has however little importance as shear stresses σ_{ST}, σ_{TL} and σ_{SL} remain small. $R(p)$ represent the plastic hardening of the undamaged material (shown on fig. 4) and p the von Mises accumulated plastic strain.

D and σ_1 are material parameters related to void growth. $D = 2$ and $\sigma_1 = 260$ MPa were used and correspond to the values recommended in [ROU 87]. The plastic strain rate tensor is obtained using the normality rule as: $\underline{\dot{\varepsilon}}^p = \lambda \partial \Phi / \partial \underline{\sigma}$ where λ is the plastic multiplier. The evolution of the void volume fraction f is given by mass conservation:

$$\dot{f} = (1 - f)\text{tr}\underline{\dot{\varepsilon}}^p.$$ [3]

The initial porosity f_0 is taken equal to the volume fraction of coarse particles which are assumed to debond at the onset of plasticity: $f_0 = 0.12\%$ [HER 98]. Using these parameters, ductility is however overestimated. Based on the observation that smaller precipitates can play a role in the fracture process, strain controlled nucleation was used in the model. The nucleated effective porosity f_n is given by

$$\dot{f}_n = A_n \dot{p}.$$ [4]

The total effective porosity f_t appearing in eq. 1 is defined as the sum $f_t = f + f_n$. Considering that nucleation starts when a given amount of plastic strain has been reached, A_n will be written as: $A_n = A_0 H(p - p_0)$ where $H(\cdot)$ is the Heavyside function and A_0 and p_0 are parameters to be adjusted. Different values for A_0 and p_0 will be used depending on the specimen type.

3.2. *Computational procedures*

FE calculations are performed using the software Zébulon [BES 98]. Constitutive equations are integrated using a fully implicit scheme which allows the calculation of the consistent tangent matrix [SIM 85]. An updated Lagrangian formulation is used; the Jauman stress rate is used to define the objective stress rate; constitutive equations are expressed in the associated corotational frame [LAD 80].

In order to reduce the number of degrees of freedom, mixed 2D/3D meshes are used. Geometrical symmetries are also accounted for. 20 nodes (3D) bricks with reduced integration (8 Gauss points) are used to model regions of crack extension. The 2D parts are freely meshed using 6 or 8 nodes plane stress elements (see 4.2.1). In order to reduce the number of elements, computations exploit the initial geometrical symmetries of the various specimens. This symmetry is however lost due to localization as evidence by the fracture surfaces. Accounting for this effect would require twice as much elements for a given mesh size.

The material is considered as broken as f_t reaches 85%. The behavior is then considered as elastic with a very low Young's modulus (1 MPa) as proposed in [LIU 94]. An element containing more than 5 broken Gauss points is automatically removed by checking this condition after each time increment.

3.3. *Results and discussion*

3.3.1. *Smooth and U–notched specimens*

Simulated macroscopic responses and fracture modes for smooth and U–notched specimens are compared with experimental results in fig. 4 and fig. 5 (F: force, S_0 initial minimum cross section, L_0, δ_0: initial gauge length, ΔL: elongation, $\Delta\delta$: notch opening displacement (see fig. 1)). All simulations were carried out using $A_0 = 0.5$ and $p_0 = 0.35$.

Smooth specimens: The macroscopic response of the specimen and the fracture plane are well reproduced. Failure occurs after the onset of necking. The fracture surface corresponds to a plane whose normal lies in the L—S plane. The angle θ between the normal and the L—direction is about 45°. The simulation was also performed assuming an isotropic plastic behavior; in this case the normal also lies in the L—S plane with a smaller value for θ which is close to localization angle under plane stress in an isotropic incompressible material (35.26°) usually observed in the L—T plane. The fact that localization still occurs in the L—S plane is likely related to the relatively small width of the specimen. Note however that due to the plastic anisotropy, $\varepsilon_{ss}^p < \varepsilon_{TT}^p$ which favors localization in the L—S plane [RUD 75].

U–notched specimen: Rupture of U–notched specimens is very similar to failure in smooth specimens. One single fracture plane is observed which also makes a 45°
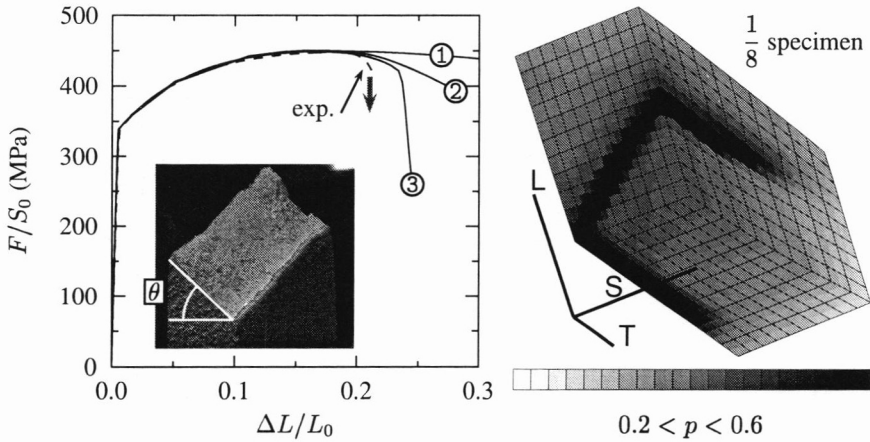
Figure 4. *Simulation of the rupture of tensile specimens. Left: Macroscopic response: (1) no damage, no necking, (2) no damage, necking, (3) damage and necking. The arrow indicates the experimental rupture. The photograph shows the experimental fracture surface ($\theta \approx 45°$). Right: Values of the plastic deformation at Gauss points showing the localization into slant fracture*

angle in the L—S plane. Macroscopic behavior as well as fracture plane are well reproduced by the FE simulation (fig. 5).

REMARKS: For both samples, FE simulations were carried out using various values for both A_0 and p_0 as well as different mesh sizes. Very similar results are obtained using more than 5 elements to mesh the S—direction (10 are used on fig. 4 and 5). The influence of p_0 and A_0 is limited for values of p_0 larger than 0.3. This indicates that the onset of failure of smooth and U–notched specimens is essentially controlled by necking and void growth. Accounting for rapid damage by nucleation is only needed to model final failure.

3.3.2. V–notched and Kahn specimens

In V–notched and Kahn specimens, the sharp notch generates strong stress and strain gradients so that a higher mesh size sensitivity is to be expected. Transition from flat to slanted fracture is experimentally observed. In this work, the emphasis was put on the modeling of this 3D phenomenon. Preliminary plane strain calculations have shown that a slanted crack path can be obtained provided a sufficiently fine mesh is used. In addition, elements should have a square shape at the onset of damage and strain localization. 3D meshes were designed according to these results.

Fig. 6 shows the crack path obtained with 7 elements in the S–direction using various values of A_0 and $p_0 = 0.2$. It is shown that increasing A_0 leads to an increase
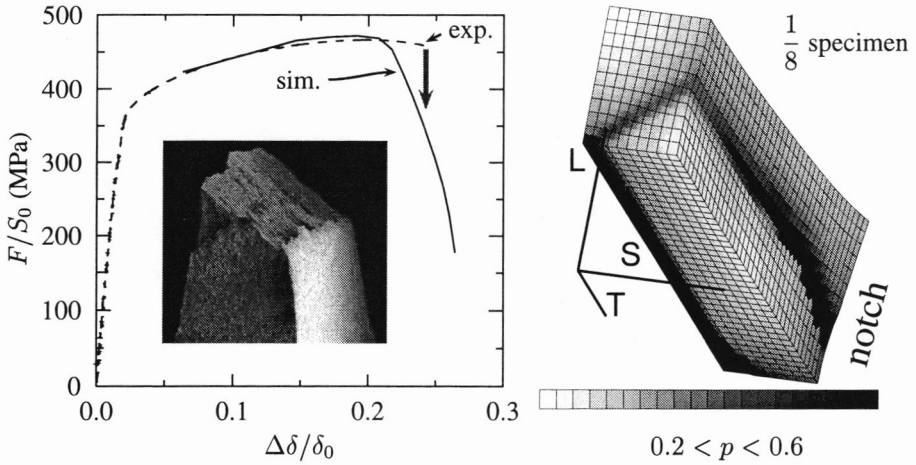
Figure 5. *Simulation of the rupture of U–notched specimens. Left: Macroscopic response (the arrow indicates the experimental rupture). Right: Values of the plastic deformation at Gauss points showing slant fracture*

of the flat fracture area. High values of A_0 generate a highly damaged zone which remains limited to one element so that crack deflection is not possible. A similar trend is obtained with increasing p_0. In this case the low hardening rate of the material limits the size of zones where p is higher than p_0.

Fig. 7 (calculation done with $A_0 = 0.5$ and $p_0 = 0.2$) indicates the values of the stress triaxiality ratio τ ahead of the crack tip after the initiation of the flat crack area. Values as high as 1.6 are obtained showing that plane stress conditions are not met; in that case the maximum value of the stress triaxiality is equal to $\frac{2}{3}$. However this maximum value remains smaller than values obtained under plane strain which lie in the range 2.5—3.0. Fig. 7 also shows details of the flat to slanted fracture transition.

$$A_0 = 0.5 \quad A_0 = 0.75 \quad A_0 = 1.0 \quad A_0 = 1.5 \quad A_0 = 2.0$$
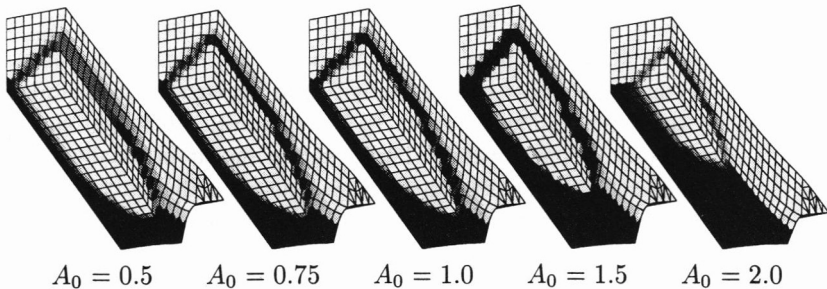
**Figure 6.** *Effect of A_0 on the flat to slanted fracture transition ($p_0 = 0.2$)*
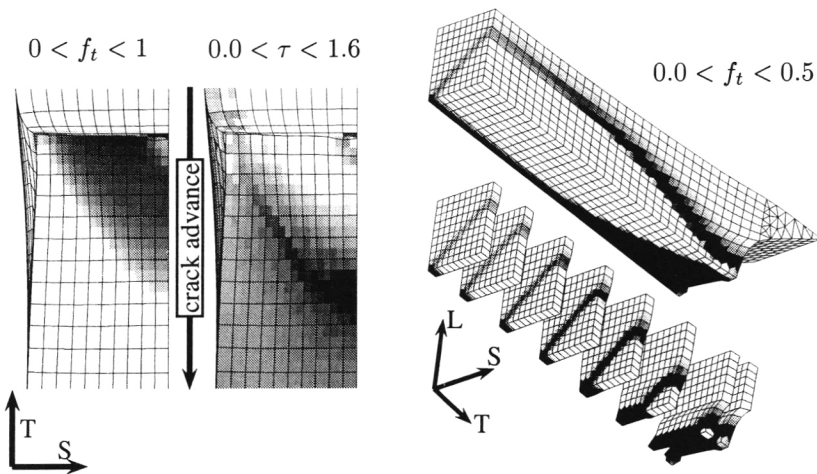
Figure 7. *Left: Gauss point value of damage (f_t) and stress triaxiality (τ) at crack initiation. Right: Final crack path showing details of the flat to slanted fracture transition. 10 elements are used in the S—direction, $A_0 = 0.5$, $p_0 = 0.2$*

The calculation qualitatively reproduces the experimental results shown in fig. 2 but overestimates the size of the flat region. The zone of normal fracture is smaller when using a smaller mesh size (e.g. fig. 6) but still larger than what is experimentally observed (fig. 2).

Simulations of the Kahn specimen are shown in fig. 8. Calculations with 5, 7 and 10 elements along the S—direction using $A_0 = 0.5$ and $p_0 = 0.2$ were performed. Decreasing the element size leads to a smaller crack growth resistance as it is expected due to the softening behavior of the material; however simulations overestimate the experimental data. For a given element size, meshing one half of the specimen (i.e. not accounting for the initial symmetries) would also reduce the simulated crack growth resistance. Faster crack growth can also be obtained by modifying the void nucleation parameters. As an example fig. 8 shows the macroscopic response obtained for $p_0 = 0.15$. Although fractographic examinations have shown that failure mechanisms change with increasing defect severity, such a low value is unlikely to be realistic. An other fitting strategy would be to increase p_0 and A_0 (i.e. delay onset of nucleation and increase nucleation rate); this however leads to flat fracture as the mesh is then too coarse to correctly capture the deformation and damage fields.

Mesh size plays a critical issue in modeling crack advance. It is often considered as a material parameter which needs to be adjusted [ROU 87, GUL 00]. Using nodular cast iron having the same volume fraction of nodules but different particle sizes, it has been shown that ductility decreases with decreasing interparticle spacing and that this effect can be modeled using meshes of decreasing sizes [STE 98]. In this
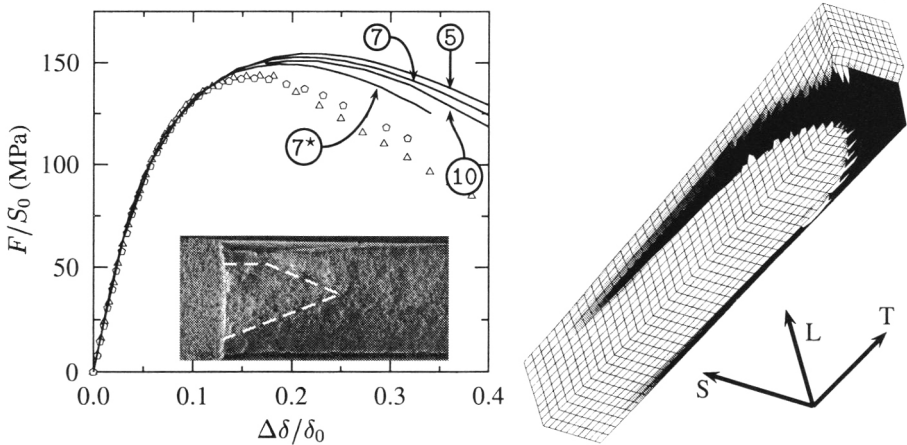
Figure 8. *Left: Force—notch opening curves using 5, 7 and 10 elements to mesh the thickness direction (S) using $A_0 = 0.5$ and $p_0 = 0.2$. 7^* corresponds to 7 elements with $p_0 = 0.15$. Points are experimental data. On the photograph, the normal fracture zone is within the white dashed line. Right: Simulated crack path using 10 elements in the S—direction*

study, fractographies have shown (fig. 2) that the mean distance between iron/copper particles is in the range 10—20 μm which is significantly smaller than the mesh size used in the present calculations ($\approx 80\mu$m). However using such a small mesh size would require a much larger computational effort (both CPU time and memory size). Note also that the use any non–local damage model would indeed require a smaller mesh size than the mesh size needed to fit the experiments using a local theory. In order to reproduce the experimental load—displacement curves on Kahn specimens, nucleation parameters can be changed to obtain a faster damage kinetic; in that case the normal to slant fracture transition cannot be modeled so that the benefit of 3D calculations is lost.

4. Cohesive zone model for plane stress state

In the previous section, it has been shown that the 3D–modeling of crack growth along a slanted path requires a large number of elements. This approach does not appear as suitable in the case of large panels; in this case a simplified 2D–modeling has to be developed. Several possibilities are however possible: (i) adjust Rousselier parameters in the plane stress case, (ii) use CTOA or CTOD, (iii) describe the crack path as a damageable interface. In all cases the actual stress state at the crack tip will not be accurately described (for instance the stress triaxiality will be underestimated).

It becomes indeed impossible to represent the slanted crack path. It is therefore likely that the associated material parameters will be geometry dependent [SIE 99].

4.1. Cohesive zone model

In the present investigation, a simplified treatment of crack growth is proposed based on a cohesive zone model. This type of model describes the material damage and separation along a surface [NEE 92]. For all specimens, the crack is assumed to stay in the initial plane of symmetry. In that case, only normal separation is to be considered. The mechanical behavior of the interface is described using a constitutive relation relating the normal component of the stress vector on the interface (σ_n) to the normal opening of the interface (δ_n). The following relation will be used in this study:

$$\sigma_n = \sigma_{\max} \frac{16e^2}{9} \frac{\delta_n}{\delta_c} \exp\left(\frac{16e}{9} \frac{\delta_n}{\delta_c}\right) \qquad [5]$$

where $e = \exp(1)$. δ_c and $\sigma_{\max}$ are two adjustable parameters of the model. $\sigma_{\max}$ represents the maximum stress carrying capacity of the interface. δ_c is a characteristic length. The function $\sigma_n(\delta_n)$ is shown on figure 9–(a). The fracture energy per unit surface Γ is given by:

$$\Gamma = \int_0^\infty \sigma_n \, \mathrm{d}\delta_n = \frac{9}{16}\sigma_{\max}\delta_c. \qquad [6]$$

In practice, it will be considered that the interface is broken (i.e. $\sigma_n = 0$) when $\delta_n \geq \delta_c$ so that the actual fracture energy is reduced by 4.6%.

4.2. Computational procedures

4.2.1. Plane stress elements

Plane stress [along the z–direction] conditions are usually taken into account by rewriting the material constitutive equations so that the condition $\sigma_{zz} = 0$ is enforced. However this method requires to modify the implementation of every material behavior. Another strategy, which requires more computational time but less programming, testing and maintenance efforts, relies of the implementation of plane stress elements [BES 97, BES 98]. These elements have the usual nodal degrees of freedom (displacements) and additional degrees of freedom (e_{zz}^i) representing the transformation gradient along the z–direction at each integration point ($i = 1 \ldots$ number of Gauss points): $e_{zz}^i = \Delta w / w_0$ (w_0 initial thickness, Δw thickness variation). The principle of virtual work is written in the current (end of time increment) configuration in order to derive the reactions associated to the different degrees of freedom. It can then be shown that the reaction R_e^i corresponding to each additional degree of freedom is equal to $R_e^i = \sigma_{zz}\omega^i$ where ω^i is the volume associated to the corresponding Gauss point. In the absence of prescribed values for

(a)   ● Node   **(b)**

                                                           ○ Gauss point
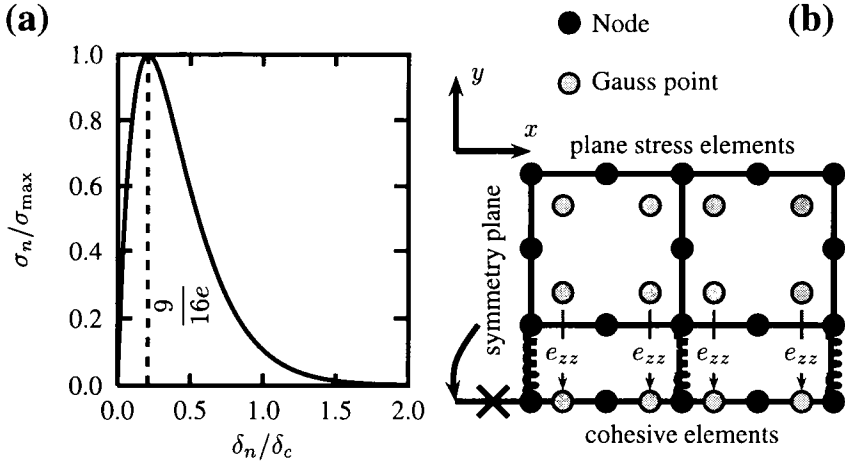
Figure 9. *(a) Traction–separation law (eq. 5). (b) Cohesive zone elements with surrounding plane stress elements*

e^i_{zz} or applied values of σ_{zz} (e.g. pressure field), the force equilibrium requires that $R^i_e = 0$, so that the plane stress condition is enforced at each Gauss point.

4.2.2. Cohesive zone elements

Cohesive zone elements are placed along the crack path and embedded in a surrounding of eight nodes large deformation plane stress elements with reduced integration (4 Gauss points). CZ elements have 6 nodes and 2 integration points. Due to symmetry, surface integrals have to be evaluated on the line of symmetry (figure 9–(b)). The virtual work for each CZ element is written as (t' denotes the end of the time increment):

$$\delta w = \int_{S_{t'}} \sigma_n \delta^\star_n \, dS_{t'} \qquad [7]$$

where $\delta^\star_n$ denotes a virtual normal displacement. The surface integral is computed accounting for the deformation of the symmetry plane but also for the sheet thickness reduction. This is done by associating each Gauss point of the CZ elements to the nearest Gauss point of the continuum plane stress elements whose thickness reduction is then used to evaluate the surface integral. Tests have shown the importance of accounting for thickness reduction. In the case of constant thickness CZ elements a slight increase of the cohesive strength or a slight modification of the crack tip constraint can result in the localization of the plastic deformation in the above lying continuum elements with no crack advance. The calculation is then equivalent to the reference elastoplastic large deformation computation without CZ.
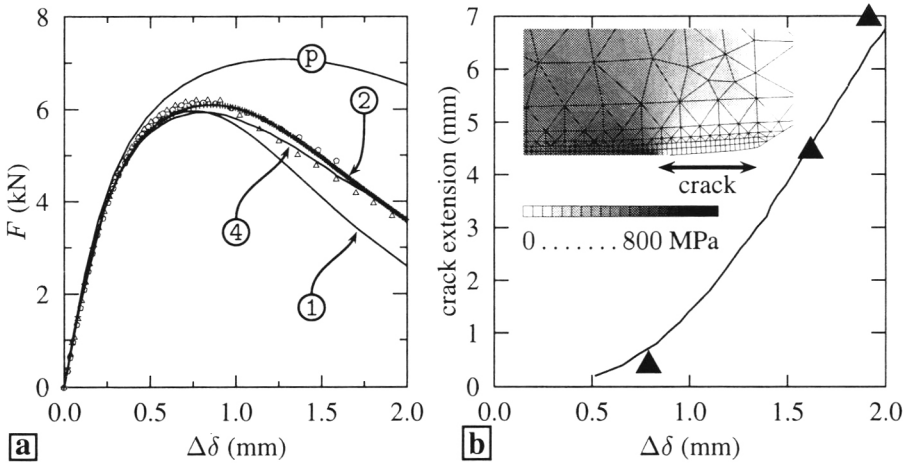
Figure 10. *Simulation of the Kahn specimen using the CZM: (a) Force vs. notch opening for different mesh sizes: 1:* $100 \times 100 \ \mu m^2$. *2:* $200 \times 200 \ \mu m^2$, *4:* $400 \times 400 \ \mu m^2$; *p: no crack growth. (b) Crack extension vs. notch opening (*$200 \times 200 \ \mu m^2$ *mesh). Contour map shows the stress (*σ_{22}*) in the loading direction. (Points represent experimental data)*

4.3. Results

The load—notch opening curve was adjusted using the following parameters: $\sigma_{max} = 720$ MPa, $\delta_c = 80 \ \mu m$. Results of the simulations shows a good agreement for both the macroscopic response (fig. 10–(a)) and crack advance (fig. 10–(b)). The macroscopic response is also compared to the response obtained without CZ. In that case failure occurs by plastic necking. Calculations were performed with an element size of $200 \mu m \times 200 \mu m$ and using a coarser ($400 \mu m \times 400 \mu m$) and finer ($100 \mu m \times 100 \mu m$) mesh. Results obtained using $200 \mu m$ and $400 \mu m$ differ only slightly whereas a faster crack advance is obtained with $100 \mu m$. This is due to the larger deformations that are computed in that case at the crack tip so that necking (and therefore stresses) is overestimated. However mesh size dependence remains smaller than in the case of CDM (section 3).

5. Summary

Ductile tearing of Aluminum 2024 sheets has been studied. The following results were obtained:

Experiments. Experiments were conducted on smooth and moderately notched specimens as well as severely notched samples. The plastic behavior is anisotropic.

Fractography shows that failure mechanisms change between these two sets of specimens with an increase of void growth in the second case. The crack path is slanted for moderately notched specimens whereas a transition from normal to slant fracture is observed on the second set.

3D modeling using CDM: 3D modeling using an extension of the Rousselier model to plastically anisotropic material was used to represent the experimental results. Strain controlled nucleation was also modeled. On the one hand, failure of tensile and U-notched specimen is essentially controlled by necking and results depend only slightly on the nucleation parameters. In that case, experimental results can be well described. On the other hand, nucleation and mesh size play a very important role in the case of V–notched and Kahn specimens. The main features of ductile tearing (in particular the normal to slant fracture transition) are qualitatively described but the load is overestimated. Adjusting the nucleation parameters in order to obtain the experimental load leads to a flat crack path. This is attributed to the relatively coarse mesh needed to perform the 3D calculations. It is believed that using a finer mesh would allow to correctly describe the load and the crack path and to use material parameters closer to those obtained on moderately notched specimens. Simulations show that stress triaxiality levels reached ahead of the crack tip are much higher than those obtained under plane stress conditions.

2D modeling using CZM: In order to overcome the difficulties encountered using the 3D CDM modeling, a simplified model using CZ elements modified to account for necking in the plane stress case has been adopted. Good results are then obtained on Kahn specimens; however based on the results presented in [SIE 99] the transferability of these parameters to other cracked geometries is questionable.

6. References

[BES 97] BESSON J., FOERCH R., "Large scale object-oriented finite element code design", *Computer Methods in Applied Mechanics and Engineering*, vol. 142, 1997, p. 165-187.

[BES 98] BESSON J., FOERCH R., "Application of object-oriented programming techniques to the finite element method. Part I- General concepts", *Revue européenne des éléments finis*, vol. 7, num. 5, 1998, p. 535-566.

[GRA 00] GRANGE M., BESSON J., ANDRIEU E., "An anisotropic Gurson model to represent the ductile rupture of hydrided Zircaloy-4 sheets", *Int. J. Fracture*, vol. 105, num. 3, 2000, p. 273-293.

[GUL 99] GULLERUD A., DODDS R., HAMPTON R., DAWICKE D., "Three dimensional modeling of ductile crack growth in thin sheet metals: computational aspects and validation", *Eng. Fracture Mechanics*, vol. 63, 1999, p. 347-373.

[GUL 00] GULLERUD A., GAO X., DODDS JR R., HAJ-ALI R., "Simulation of ductile crack growth using computational cells: numerical aspects", *Eng. Fracture Mechanics*, vol. 66, 2000, p. 65-92.

[HER 98] HERMANN G., Déchirure ductile de tôles minces d'un alliage Aluminium-Cuivre, report , 1998, Pechiney CRV.

[LAD 80] LADEVÈZE P., Sur la théorie de la plasticité en grandes déformations, report , 1980, Rapport interne No. 9, LMT, ENS Cachan.

[LIU 94] LIU Y., MURAKAMI S., KANAGAWA Y., "Mesh-dependence and stress singularity in finite element analysis of creep crack growth by continuum damage mechanics approach", *Eur. J. Mech, A/Solids*, vol. 13, num. 3, 1994, p. 395-417.

[NEE 90] NEEDLEMAN A., "An analysis of tensile decohesion along an interface", *J. Mech. Phys. Solids*, vol. 38, 1990, p. 289-324.

[NEE 92] NEEDLEMAN A., "An analysis of decohesion along an imperfect interface", *Int. J. Fracture*, vol. 40, 1992, p. 1377-1397.

[O'D 92] O'DOWD N., SHIH C., "Family of crack-tip fields characterized by a triaxiality parameter-II. Fracture Applications", *J. Mech. Phys. Solids*, vol. 40, num. 8, 1992, p. 939-963.

[RIC 68] RICE J., "A path independent integral and the approximate analysis of strain concentration by notched and cracks", *J. Appl. Mech.*, vol. 35, 1968, p. 379.

[ROU 87] ROUSSELIER G., "Ductile fracture models and their potential in local approach of fracture", *Nuclear Engineering and Design*, vol. 105, 1987, p. 97-111.

[RUD 75] RUDNICKI J., RICE J., "Conditions for the localization of deformation in pressure-sensitive dilatant materials", *J. Mech. Phys. Sol.*, vol. 23, 1975, p. 371-394.

[SIE 99] SIEGMUND T., BROCKS W., "Prediction of the work of separation and implications to modelling", *Int. J. Frac.*, vol. 99, 1999, p. 97-116.

[SIM 85] SIMO J., TAYLOR R., "Consistent tangent operators for rate-independent elastoplasticity", *Computer Methods in Applied Mechanics and Engineering*, vol. 48, 1985, p. 101-118.

[STE 98] STEGLICH D., BROCKS W., "Micromechanical modelling of damage and fracture of ductile materials", *Fatigue Fract. Engng Mater. Struct.*, vol. 21, 1998, p. 1175-1188.

[SUN 88] SUN D., SIEGELE D., VOSS B., SCHMITT W., "Application of local damage models to the numerical analysis of ductile rupture", *Fatigue and Fracture of Engineering Materials and Structures*, vol. 12, 1988, p. 201-212.

[TUR 92] TURNER C., "A re-assessment of ductile tearing resistance. Part I: The geometry dependence of *J-R* curves in fully plastic bending. Part II: Energy dissipation rate and associated *R*-curves in fully plastic bending.", *Fracture behavior and design of materials and structures*, ECF 8, 1992, p. 933-968.